Hyperspectral terahertz microscopy via nonlinear ghost-imaging

Article (Published Version)

optica

Hyperspectral terahertz microscopy via nonlinear ghost imaging

Luana Olivieri,[1] Juan S. Totero Gongora,[1] Luke Peters,[1] Vittorio Cecconi,[1] Antonio Cutrona,[1,2] Jacob Tunesi,[1] Robyn Tucker,[1] Alessia Pasquazi,[1] and Marco Peccianti[1,*]

[1]Emergent Photonics (EPic) Laboratory, Department of Physics and Astronomy, University of Sussex, Brighton, UK
[2]Department of Engineering, University of Palermo, Palermo, Italy
*Corresponding author: m.peccianti@sussex.ac.uk

Received 25 October 2019; revised 9 January 2020; accepted 9 January 2020 (Doc. ID 381035); published 19 February 2020

Ghost imaging, based on single-pixel detection and multiple pattern illumination, is a crucial investigative tool in difficult-to-access wavelength regions. In the terahertz domain, where high-resolution imagers are mostly unavailable, ghost imaging is an optimal approach to embed the temporal dimension, creating a "hyperspectral" imager. In this framework, high resolution is mostly out of reach. Hence, it is particularly critical to developing practical approaches for microscopy. Here we experimentally demonstrate time-resolved nonlinear ghost imaging, a technique based on near-field, optical-to-terahertz nonlinear conversion and detection of illumination patterns. We show how space–time coupling affects near-field time-domain imaging, and we develop a complete methodology that overcomes fundamental systematic reconstruction issues. Our theoretical-experimental platform enables high-fidelity subwavelength imaging and carries relaxed constraints on the nonlinear generation crystal thickness. Our work establishes a rigorous framework to reconstruct hyperspectral images of complex samples inaccessible through standard fixed-time methods.

https://doi.org/10.1364/OPTICA.381035

1. INTRODUCTION

The reconstruction of complex field distributions in space and time is a challenge in many domains, with a significant transversal impact in fields beyond optics, such as microwave beam steering, ultrasound imaging, and biology [1–9]. On another front, hyperspectral imaging has a pivotal assessment role in many disciplines, as it allows one to determine the 2D morphology of an absorption spectrum [10–12]. Hyperspectral imaging assumes a broader probing significance in time-resolved systems; in particular, the delay of each frequency component can be profitably used to access the 3D morphology of the spectral phase response of a target, i.e., its spatially resolved complex dielectric function. Modern photonic approaches have produced essential breakthroughs in medicine, biology, and material science imaging [12–16]. In this context, the ability to reconstruct the time-domain waveforms provides direct access to the field [17]; although these approaches are well established in microwave and ultrasound imaging [2,5–7], they are sensibly less diffused in photonics. Terahertz (THz), in this regard, has emerged as one of the most relevant photonics frameworks in which the time evolution of a field amplitude is experimentally accessible. Indeed, THz time-domain spectroscopy (TDS) has played a pivotal role in establishing THz as an independent research field [18–21].

Single-pixel imaging approaches find their origin in domains where single-point detectors outperform detector-arrays in terms of specifications or availability [22,23]; for this reason, they have attracted interest also in the THz community [24–26]. In photonics, these methods have unlocked the powerful ability to add multiple dimensions and novel functionalities to simple spatial probing, enabling several breakthroughs in classical and quantum imaging [25,27–32]. In its most modern connotation, ghost imaging (GI) is a form of computational imaging that employs the sequential illumination of an object with a set of predetermined patterns [23,33–37].

In terms of accessing newly emerging wave domains, such as THz, GI offers the option of closing relevant technological gaps while raising new challenges, such as the limited availability of THz spatial light modulators (SLMs) and the coarse diffraction limit [25].

The combination of single-pixel imaging and TDS provides the exciting possibility of exploiting novel space–time computational imaging approaches [31,32], and the TDS-GI has been recently proposed as viable for THz imaging [38–42]. The THz field can be densely sampled in space, giving access to subwavelength microscopy when an object is exposed to the near field of a THz source, detector, or mask. Besides its potential practical impact in THz microscopy, GI microscopy provides an accessible fundamental framework for investigating time-resolved imaging in the presence

of strong spatiotemporal coupling, a dominant condition in the near-field domain.

In this paper, we experimentally implement an imaging protocol based on the time-resolved nonlinear ghost imaging (TNGI), which we have recently theoretically proposed as a single-pixel imaging method where a set of nonlinear wavelength transformations are inserted in both the illumination and detection chains [43]. We generate the THz patterns used for the GI reconstruction by nonlinear conversion of spatially modulated optical pulses in a quadratic medium. Leveraging the time-dependent field detection, as opposed to the intensity detection usually implemented in the optics GI-equivalent, we implement the detection in the Fourier plane, effectively acquiring the average value of the scattered field. With this approach, the system resolution is effectively independent of the numerical aperture of the detection system, in sharp contrast with standard single-pixel approaches working in optics. We test our time-dependent THz microscope on benchmark images, showing the capability of our system to extract the spectrally resolved morphology, such as the water content in a leaf.

Most importantly, we demonstrate near-field, coherent hyperspectral imaging in a regime where spatiotemporal coupling is strongly evident. We experimentally show that, in this regime, the image information is inherently inaccessible when the reconstruction is performed at fixed-time slices of the transmitted field, as the traditional isotime imaging approaches become affected by errors and artifacts. We show experimentally that in the near field, the full spatiotemporal signal is required to preserve space–time imaging, and we provide a methodology, which we refer to as "space–time refocusing" for high-fidelity reconstruction. Interestingly, we also show experimentally that the thickness of the generation crystal does not preclude significantly higher resolutions (as in some of the proposed THz-GI approaches).

2. METHODS: THE TNGI

We formulated the TNGI as a single-pixel imaging approach based on the time-resolved detection of the electromagnetic field scattered by a sample, as opposed to the standard formulation of GI that relies on the time-averaged field intensity [43]. Without loss of generality, the TNGI describes the optical and morphological features of a sample through a spatiotemporal transfer function $T_{\text{sample}}(x, y, t)$ that is reconstructed through a sequence of measurements as follows:

$$T_{\text{sample}}(x, y, t) = \langle C_n(t) I_n(x, y)\rangle_n - \langle C_n(t)\rangle_n \langle I_n(x, y)\rangle_n, \quad (1)$$

where $I_n(x, y)$ is the intensity distribution of the nth incident optical pattern, and $\langle \cdots \rangle_n$ is the average over the distribution of patterns. In Eq. (1), the expansion coefficients $C_n(t)$ are defined as

$$C_n(t) = \int E_n^+(x, y, t)\mathrm{d}x\mathrm{d}y, \quad (2)$$

and correspond to the spatial average of the complex electric field $E_n^+(x, y, t)$ transmitted by the sample and acquired by TDS detection (see Supplement 1 Section S3). Note that Eq. (1) is closely related to the linear formulation of standard GI, where the incident and scattered intensities are linearly related. Such a similarity is a direct consequence of the optical-to-THz conversion taking place in quadratic media, where the generated THz field is expressed as

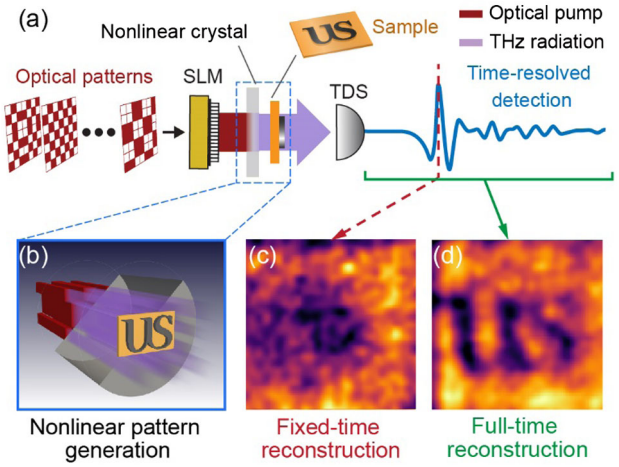

Fig. 1. Conceptual description of the TNGI approach. (a) Key experimental components and methodology; (b) volumetric representation of the nonlinear generation of THz patterns; (c) fixed-time reconstruction with a field of view 2 mm × 2 mm and 32 × 32 spatial sampling; (d) backpropagated hyperspectral image, averaged between 1 and 2 THz.

$$E_{\text{THz}}(x, y) \propto \chi^{(2)} I_n(x, y), \quad (3)$$

where $\chi^{(2)}$ is the second-order nonlinear susceptibility of the nonlinear medium. The capability of directly controlling the THz field by acting on the incident optical intensity is an essential feature of our approach, as in casting Eq. (1) we do not require any assumption stemming from the binary nature of the illumination (as required, e.g., in mask-based GI [39–42]). It is also worth noting that, differently from the standard GI formulation, the coefficients in Eqs. (1) and (2) are built up by coherent measurements of the electric field, and they do not represent the scattered intensity.

The principal elements of our experimental implementation of the TNGI are shown in Fig. 1. We impressed a series of intensity patterns on an ultrafast optical beam ($\lambda = 800$ nm, repetition rate 1 kHz, pulse duration 75 fs) using a commercial wavefront-shaping device. In our experiments, we employed both a binary amplitude digital micromirror device (DMD) and a phase-only liquid crystal on silicon (LCoS) SLM. We converted the optical pattern to a THz field distribution $E_{\text{THz}}(x, y, t)$ through nonlinear optical rectification in a quadratic crystal (ZnTe) of thickness z_0. The generated THz pattern sampled different targets (in our experiments different metallic masks and dielectrics) placed in proximity to the crystal surface, and the average transmitted field was measured through electro-optic (EO) detection. In our THz implementation, the $C_n(t)$ coincide with the electric field detected via TDS at the center of the Fourier plane (i.e., at $k_x = k_y = 0$) [44]. As an image-reconstruction protocol, we exploited a Walsh–Hadamard encoding scheme (with "Russian doll" ordering [45]) based on binary amplitude patterns, which is known to maximize the SNR of single-pixel imaging schemes [39]. A detailed schematic and further details on the optical setups are included in the supplementary information (SI).

The use of nonlinear conversion to generate THz patterns provides a series of features when developing a single-pixel TDS imaging scheme. First, the ability to control the THz field distribution by shaping the optical field, as expressed by Eq. (3), allows us to generate patterns with subwavelength resolution when compared to the THz wavelength (300 μm, at 1 THz). The resolution of the optical pattern $I_n(x, y)$ is ultimately bound by the optical

diffraction limit and the numerical aperture of the optical setup. Second, the SNR of the detected THz signal increases linearly with the incident optical intensity. Finally, there is perfect temporal coherence and spatial correspondence between the pump pulse and the distribution of THz sources. Temporal and spatial coherence is a direct consequence of the nonlinear conversion process and has significant consequences for our abililty to image samples in challenging experimental conditions. An open issue in THz-GI concerns the impact of the distance between the THz pattern source and the sample, as required when assessing the transmission from a sample placed on a holding substrate. As discussed in Refs. [39,43], the near-field propagation of subwavelength patterns exhibits spatiotemporal coupling, altering the spatial and temporal features of the pattern [46]. Under these conditions, the sampling function impinging on the object is not the original, predetermined pattern, but its space–time "propagated" version. Such discrepancy introduces a systematic and uneliminable error in determining the scattered waveform from the object using a

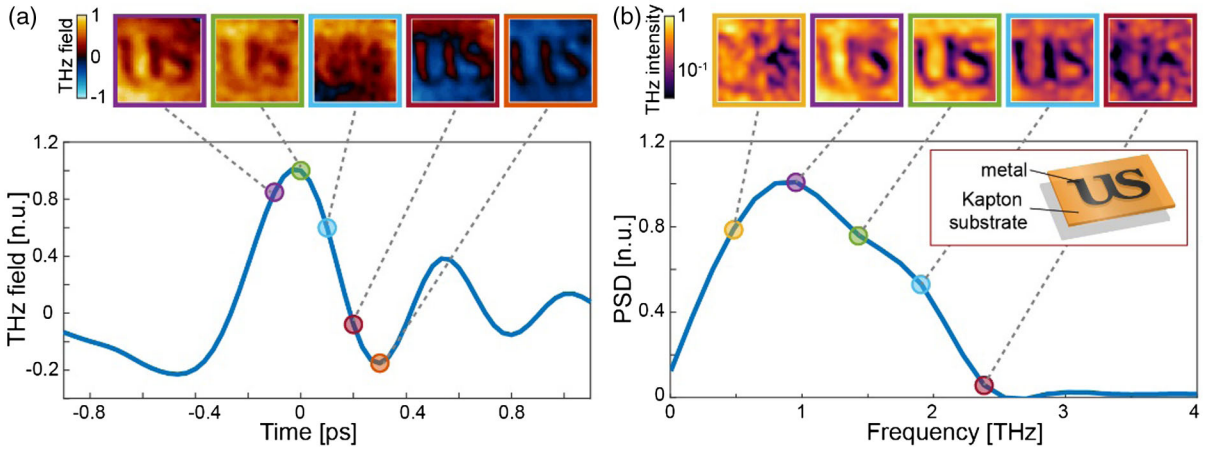

Fig. 2. Spatiotemporal image of a metallic sample. (a) Temporal response of the metallic sample with fixed-time image reconstructions. It is worth noting that field evolution (color change) can be appreciated underneath the metallic mask as the structure resonance produces a secondary emission. (b) Spectral response with hyperspectral images. The field of view was 2 mm × 2 mm with a 16 × 16 spatial sampling.

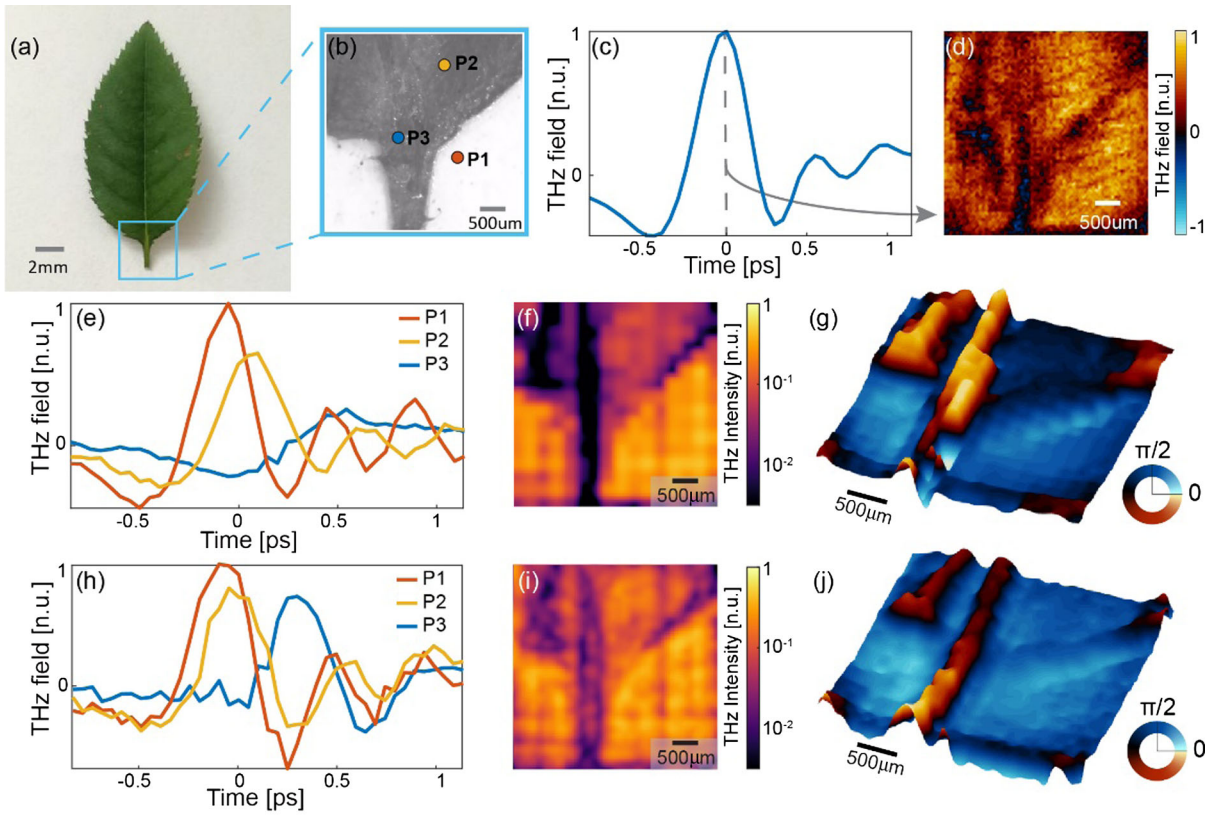

Fig. 3. Hyperspectral image of a leaf. (a) Optical image of the leaf; (b) microscope image; (c) temporal response of the field transmitted by the leaf; (d) fixed-time reconstruction (128 pixels × 128 pixels); (e) local temporal response of the fresh leaf in the points indicated in (b); (f) hyperspectral image of a fresh leaf at 1.5 THz (16 pixels × 16 pixels); (g) phase image of the fresh leaf, obtained without phase unwrapping of the experimental data; (h)–(j) same as the previous panel for a dried leaf (32 pixel × 32 pixel images). All the images correspond to a field of view of 4 mm × 4 mm.

time-sliced (or isotime) imaging. While the effect of spatiotemporal coupling could be reduced when the sample distance from the sources is much smaller than the resolution targeted (i.e., by employing a thin patterning substrate), the error introduced by diffraction (and by the interaction with samples with complex transmission properties) is always present. Such an error is not quantifiable in the case of single time-slice acquisition, and it cannot be represented by standard definitions of SNR employed in image analysis. The combination of optical coherence and direct field detection allows us to reverse the effects of spatiotemporal coupling, to obtain the correct time-domain reconstruction of a sample within one wavelength of distance, and to perform coherent hyperspectral imaging through TNGI.

3. EXPERIMENTAL RESULTS: HYPERSPECTRAL IMAGING

As a first case study, in Fig. 2 we present the 2 mm × 2 mm spatiotemporal image of a metallic structure deposited on a 50 μm Kapton substrate. The image was retrieved by shaping the optical illumination with a binary DMD and by placing the metallic structure in the proximity of a $z_0 = 1$ mm thick ZnTe generation crystal. We achieved analogous results using an LCoS modulator, as shown in Supplement 1 Fig. 2. By retrieving the spatiotemporal image of the sample [Fig. 2(a)], we can capture the full effects of the interaction between the THz field and its subwavelength metallic features. As can be observed at $t = 0.2$ ps, in fact, the object does not appear just as a blocking mask, but it features complex resonances from the edges of the object. The time-resolved measurement of the scattered field also allows us to reconstruct the hyperspectral image of the sample [Fig. 2(b)]. Interestingly, in our experiments, we were able to resolve features within the 50–100 μm scale even in the presence of a relatively thick generation crystal (as opposed to the typical thickness requirements in other approaches [39–42]). This is a direct consequence of the nonlinear conversion of optical patterns taking place across the entire volume of the generating crystal and not only at its surface. In this condition, the field-spatial spectra of each generating layer in the ZnTe do not mix incoherently and, differently from the linear case, allow single-pixel reconstruction of subwavelength features (see Supplement 1 Section S2 for a detailed discussion).

The access to the coherent temporal field response allowed us to reconstruct full spatiotemporal images of semitransparent samples. As a relevant example (and to credit a similar image in Ref. [20], widely considered one of the first milestones in THz imaging), we show in Fig. 3 an image of a leaf at different stages of desiccation. As can be evinced from Figs. 3(c) and 3(d), the isotime image of a semitransparent sample is significantly harder to interpret than a standard metallic mask, as the different parts of the sample induce different temporal delays and phase shifts. Nevertheless, we were able to retrieve the TDS time trace in different points of the sample [Figs. 3(e) and 3(h)] and retrieve its hyperspectral image both in terms of amplitude [Figs. 3(f) and 3(i)] and spectral phase [Figs. 3(g) and 3(j)], allowing us to reconstruct its morphology and spectral fingerprint. As relevant examples, we present data for a fresh leaf [Figs. 3(e)–3(g)] and a dried leaf [Figs. 3(h)–3(j)]. By comparing the transmission from the two samples, it is possible to assess the changes in water content, as in Ref. [20].

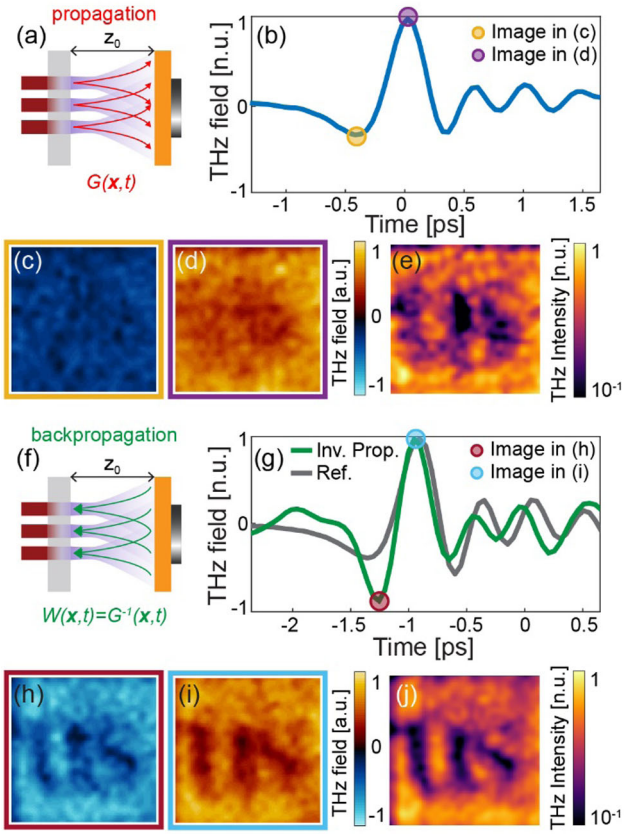

Fig. 4. Time-resolved image reconstruction: inverse propagation approach. (a) Conceptual illustration of the propagating imaging scheme: the sample is placed at $z_0 = 300$ μm from the crystal. (b) Temporal response of the sample; (c)–(d) fixed-time reconstructed images at the points indicated in (b); (e) hyperspectral image averaged between 1 and 2 THz; (f) conceptual illustration of the backpropagation scheme; (g) temporal response of the backpropagated image (green) and the temporal response without the sample (gray); (h)–(i) fixed-time reconstruction of the backpropagated image at the points indicated in (g); (j) backpropagated hyperspectral image, averaged between 1 and 2 THz. In all panels, the field of view was 2 mm × 2 mm with a 32 × 32 spatial sampling.

4. IMAGING THROUGH INVERSE PROPAGATION

The experimental results presented in Fig. 4 explore a relevant consequence of the space–time coupling in near-field TNGI. In this case, we collected the image of a metallic sample, analogous to the one in Fig. 2, but introducing a nonnegligible distance between the sample and the emitter, which includes the Kapton substrate, in a typical time-of-flight imaging case.

In these conditions, the sample morphology cannot be appreciated in any of the isotime images regardless of their temporal position [Figs. 4(c), 4(d) show some examples], or in the hyperspectral image [Fig. 4(e)], which shows a quite distorted image even if in some pixels a high contrast is reached. As theoretically demonstrated in Ref. [43], such a limitation is a direct consequence of spatiotemporal coupling, which leads to a substantial modification of the incident sampling patterns as they propagate [Fig. 4(a)]. At this stage, it should be observed that our TNGI protocol relies on the collection of the average field as performed by sampling the origin of an optical Fourier plane (i.e., $k_x = k_y = 0$). As a result, it only requires an optical system capable of collecting a very narrow spatial spectrum, and the numerical aperture of the imaging system

plays a minimal role in defining the image resolution. On the contrary, the SNR of the THz detection plays a fundamental role in resolving the vanishing near-field scattered contributions (at high spatial frequencies) for increasing values of the distance between the sample and the emitter.

With the sensitivity available, we could then backpropagate the pattern sampling function in order to "space–time refocus" the image [Fig. 4(f)] and reverse the effect of spatiotemporal coupling (see Supplement 1 Section S3 for a theoretical discussion on the inverse propagation reconstruction) [43]. This procedure allows us to retrieve the correct time-resolved image of the scattered field in the proximity of the sample, restoring the morphological and spectral features of its hyperspectral image [Figs. 4(i)–4(j)]. We argue that the inverse propagation reconstruction is a strict requirement to reconstruct the sample properties at different depths, i.e., in near-field time-of-flight imaging.

5. CONCLUSIONS

In conclusion, we performed the first experimental example of the TNGI approach exploiting a nonlinear quadratic conversion. We devised a general reconstruction method based on the linear dependence between impinging optical patterns and the detected THz time-domain field average. The approach enables hyperspectral imaging as performed in the state-of-the-art by TDS imagers. It features near-field imaging and shows relaxed constraints in terms of thickness of the nonlinear converter (our proof-of-concept exploits off-the-shelf nonlinear substrates). As predicted in Ref. [43], we demonstrated that popular isotime approaches are not suitable for near-field spatiotemporal microscopy, and this is a central issue when an object comprises elements at different optical depths. We proved experimentally that, thanks to the spatial and temporal coherence, it is possible to devise an inverse propagation operator capable of "refocusing" the image in space–time and, therefore, correctly reconstructing the hyperspectral image of the sample. We believe this work can have a substantial impact in the field of near-field imaging, especially in light of the emergence of thinner and more efficient THz emitters (e.g., spintronic substrates, surface emitters, or novel materials with exceptionally high nonlinear coefficients such as DSTMS crystals) [47–50].

Funding. European Research Council under the European Union's Horizon 2020 Research and Innovation Programme (725046); UK Engineering and Physical Sciences Research Council (EP/N509784/1, EP/S001018/1); University of Sussex (UK) ("Helena Normanton" Fellowship); University of Palermo (Italy) (mobility fellowship "Corso di Perfezionamento all'estero 2018").

Acknowledgment. This project has received funding from the European Research Council (ERC) under the European Union's Horizon 2020 research and innovation programme (grant agreement No 725046). J.S.T.G, L.P., V.C., and R.T. acknowledge the support of the European Union's "Horizon 2020" research and innovation program, grant agreement No 725046, ERC-CoG project TIMING. J.T. acknowledges the support of the EPSRC through the studentship EP/N509784/1. J.S.T.G. acknowledges funding from the Helena Normanton Fellowship of the University of Sussex, UK. A.C. acknowledges the support from the University of Palermo, Italy through the mobility fellowship "Corso di Perfezionamento all'estero 2018".

Disclosures. The authors declare no conflicts of interest.

See Supplement 1 for supporting content. The datasets for all figures are freely accessible at [51].

REFERENCES

1. D. Huang, E. A. Swanson, C. P. Lin, J. S. Schuman, W. G. Stinson, W. Chang, M. R. Hee, T. Flotte, K. Gregory, C. A. Puliafito, and A. Et, "Optical coherence tomography," Science **254**, 1178–1181 (1991).
2. L. Borcea, G. Papanicolaou, C. Tsogka, and J. Berryman, "Imaging and time reversal in random media," Inverse Probl. **18**, 1247–1279 (2002).
3. G. Lerosey, J. de Rosny, A. Tourin, and M. Fink, "Focusing beyond the diffraction limit with far-field time reversal," Science **315**, 1120–1122 (2007).
4. J. Bertolotti, E. G. van Putten, C. Blum, A. Lagendijk, W. L. Vos, and A. P. Mosk, "Non-invasive imaging through opaque scattering layers," Nature **491**, 232–234 (2012).
5. C. Errico, J. Pierre, S. Pezet, Y. Desailly, Z. Lenkei, O. Couture, and M. Tanter, "Ultrafast ultrasound localization microscopy for deep super-resolution vascular imaging," Nature **527**, 499–502 (2015).
6. I. N. Papadopoulos, J.-S. Jouhanneau, J. F. A. Poulet, and B. Judkewitz, "Scattering compensation by focus scanning holographic aberration probing (F-SHARP)," Nat. Photonics **11**, 116–123 (2017).
7. A. V. Diebold, M. F. Imani, T. Sleasman, and D. R. Smith, "Phaseless coherent and incoherent microwave ghost imaging with dynamic metasurface apertures," Optica **5**, 1529–1541 (2018).
8. Y. Rivenson, Y. Zhang, H. Günaydın, D. Teng, and A. Ozcan, "Phase recovery and holographic image reconstruction using deep learning in neural networks," Light Sci. Appl. **7**, 17141 (2018).
9. L. Li, H. Ruan, C. Liu, Y. Li, Y. Shuang, A. Alù, C.-W. Qiu, and T. J. Cui, "Machine-learning reprogrammable metasurface imager," Nat. Commun. **10**, 1082 (2019).
10. A. A. Gowen, "Hyperspectral imaging: an emerging process analytical tool for food quality and safety control," Trends Food Sci. Technol. **18**, 590–598 (2007).
11. D. Bannon, "Cubes and slices," Nat. Photonics **3**, 627–629 (2009).
12. G. Lu and B. Fei, "Medical hyperspectral imaging: a review," J. Biomed. Opt. **19**, 010901 (2014).
13. W. Jahr, B. Schmid, C. Schmied, F. O. Fahrbach, and J. Huisken, "Hyperspectral light sheet microscopy," Nat. Commun. **6**, 7990 (2015).
14. I. Amenabar, S. Poly, M. Goikoetxea, W. Nuansing, P. Lasch, and R. Hillenbrand, "Hyperspectral infrared nanoimaging of organic samples based on Fourier transform infrared nanospectroscopy," Nat. Commun. **8**, 14402 (2017).
15. X. Hadoux, F. Hui, J. K. H. Lim, C. L. Masters, A. Pébay, S. Chevalier, J. Ha, S. Loi, C. J. Fowler, C. Rowe, V. L. Villemagne, E. N. Taylor, C. Fluke, J.-P. Soucy, F. Lesage, J.-P. Sylvestre, P. Rosa-Neto, S. Mathotaarachchi, S. Gauthier, Z. S. Nasreddine, J. D. Arbour, M.-A. Rhéaume, S. Beaulieu, M. Dirani, C. T. O. Nguyen, B. V. Bui, R. Williamson, J. G. Crowston, and P. van Wijngaarden, "Non-invasive in vivo hyperspectral imaging of the retina for potential biomarker use in Alzheimer's disease," Nat. Commun. **10**, 4227 (2019).
16. F. Yesilkoy, E. R. Arvelo, Y. Jahani, M. Liu, A. Tittl, V. Cevher, Y. Kivshar, and H. Altug, "Ultrasensitive hyperspectral imaging and biodetection enabled by dielectric metasurfaces," Nat. Photonics **13**, 390–396 (2019).
17. X. Yin, B. W.-H. Ng, and D. Abbott, *Terahertz Imaging for Biomedical Applications: Pattern Recognition and Tomographic Reconstruction* (Springer, 2012).
18. D. H. Auston and M. C. Nuss, "Electrooptical generation and detection of femtosecond electrical transients," IEEE J. Quantum Electron. **24**, 184–197 (1988).
19. Ch. Fattinger and D. Grischkowsky, "Terahertz beams," Appl. Phys. Lett. **54**, 490–492 (1989).
20. B. B. Hu and M. C. Nuss, "Imaging with terahertz waves," Opt. Lett. **20**, 1716–1718 (1995).
21. N. Horiuchi, "Terahertz technology: endless applications," Nat. Photonics **4**, 140 (2010).

22. J. H. Shapiro, "Computational ghost imaging," Phys. Rev. A **78**, 061802R (2008).
23. Y. Bromberg, O. Katz, and Y. Silberberg, "Ghost imaging with a single detector," Phys. Rev. A **79**, 053840 (2009).
24. W. L. Chan, K. Charan, D. Takhar, K. F. Kelly, R. G. Baraniuk, and D. M. Mittleman, "A single-pixel terahertz imaging system based on compressed sensing," Appl. Phys. Lett. **93**, 121105 (2008).
25. C. M. Watts, D. Shrekenhamer, J. Montoya, G. Lipworth, J. Hunt, T. Sleasman, S. Krishna, D. R. Smith, and W. J. Padilla, "Terahertz compressive imaging with metamaterial spatial light modulators," Nat. Photonics **8**, 605–609 (2014).
26. T. Yuan, J. Z. Xu, and X.-C. Zhang, "Development of terahertz wave microscopes," Infrared Phys. Technol. **45**, 417–425 (2004).
27. M. Unternährer, B. Bessire, L. Gasparini, M. Perenzoni, and A. Stefanov, "Super-resolution quantum imaging at the Heisenberg limit," Optica **5**, 1150–1154 (2018).
28. A. P. Spencer, B. Spokoyny, S. Ray, F. Sarvari, and E. Harel, "Mapping multidimensional electronic structure and ultrafast dynamics with single-element detection and compressive sensing," Nat. Commun. **7**, 10434 (2016).
29. D. B. Phillips, M.-J. Sun, J. M. Taylor, M. P. Edgar, S. M. Barnett, G. M. Gibson, and M. J. Padgett, "Adaptive foveated single-pixel imaging with dynamic supersampling," Sci. Adv. **3**, e1601782 (2017).
30. B. Sun, M. P. Edgar, R. Bowman, L. E. Vittert, S. Welsh, A. Bowman, and M. J. Padgett, "3D computational imaging with single-pixel detectors," Science **340**, 844–847 (2013).
31. C. Amiot, P. Ryczkowski, A. T. Friberg, J. M. Dudley, and G. Genty, "Supercontinuum spectral-domain ghost imaging," Opt. Lett. **43**, 5025–5028 (2018).
32. H. Wu, P. Ryczkowski, A. T. Friberg, J. M. Dudley, and G. Genty, "Temporal ghost imaging using wavelength conversion and two-color detection," Optica **6**, 902–906 (2019).
33. R. S. Bennink, S. J. Bentley, and R. W. Boyd, "Two-photon" coincidence imaging with a classical source," Phys. Rev. Lett. **89**, 113601 (2002).
34. Y. Altmann, S. McLaughlin, M. J. Padgett, V. K. Goyal, A. O. Hero, and D. Faccio, "Quantum-inspired computational imaging," Science **361**, eaat2298 (2018).
35. H. Defienne, M. Reichert, J. W. Fleischer, and D. Faccio, "Quantum image distillation," Sci. Adv. **5**, eaax0307 (2019).
36. P. Caramazza, O. Moran, R. Murray-Smith, and D. Faccio, "Transmission of natural scene images through a multimode fibre," Nat. Commun. **10**, 1–6 (2019).
37. A. Lyons, F. Tonolini, A. Boccolini, A. Repetti, R. Henderson, Y. Wiaux, and D. Faccio, "Computational time-of-flight diffuse optical tomography," Nat. Photonics **13**, 575–579 (2019).
38. R. I. Stantchev, B. Sun, S. M. Hornett, P. A. Hobson, G. M. Gibson, M. J. Padgett, and E. Hendry, "Noninvasive, near-field terahertz imaging of hidden objects using a single-pixel detector," Sci. Adv. **2**, e1600190 (2016).
39. R. I. Stantchev, D. B. Phillips, P. Hobson, S. M. Hornett, M. J. Padgett, and E. Hendry, "Compressed sensing with near-field THz radiation," Optica **4**, 989–992 (2017).
40. R. I. Stantchev, J. C. Mansfield, R. S. Edginton, P. Hobson, F. Palombo, and E. Hendry, "Subwavelength hyperspectral THz studies of articular cartilage," Sci. Rep. **8**, 6924 (2018).
41. S.-C. Chen, L.-H. Du, K. Meng, J. Li, Z.-H. Zhai, Q.-W. Shi, Z.-R. Li, and L.-G. Zhu, "Terahertz wave near-field compressive imaging with a spatial resolution of over λ/100," Opt. Lett. **44**, 21–24 (2019).
42. J. Zhao, E. Yiwen, K. Williams, X.-C. Zhang, and R. W. Boyd, "Spatial sampling of terahertz fields with sub-wavelength accuracy via probe-beam encoding," Light Sci. Appl. **8**, 55 (2019).
43. L. Olivieri, J. S. Totero Gongora, A. Pasquazi, and M. Peccianti, "Time-resolved nonlinear ghost imaging," ACS Photon. **5**, 3379–3388 (2018).
44. H. Guerboukha, K. Nallappan, and M. Skorobogatiy, "Exploiting k-space/frequency duality toward real-time terahertz imaging," Optica **5**, 109–116 (2018).
45. M.-J. Sun, L.-T. Meng, M. P. Edgar, M. J. Padgett, and N. Radwell, "A Russian Dolls ordering of the Hadamard basis for compressive single-pixel imaging," Sci. Rep. **7**, 3464 (2017).
46. M. Peccianti, M. Clerici, A. Pasquazi, L. Caspani, S. P. Ho, F. Buccheri, J. Ali, A. Busacca, T. Ozaki, and R. Morandotti, "Exact reconstruction of THz sub-lambda source features in knife-edge measurements," IEEE J. Sel. Top. Quantum Electron. **19**, 8401211 (2013).
47. L. Peters, J. Tunesi, A. Pasquazi, and M. Peccianti, "High-energy terahertz surface optical rectification," Nano Energy **46**, 128–132 (2018).
48. T. Seifert, S. Jaiswal, U. Martens, J. Hannegan, L. Braun, P. Maldonado, F. Freimuth, A. Kronenberg, J. Henrizi, I. Radu, E. Beaurepaire, Y. Mokrousov, P. M. Oppeneer, M. Jourdan, G. Jakob, D. Turchinovich, L. M. Hayden, M. Wolf, M. Münzenberg, M. Kläui, and T. Kampfrath, "Efficient metallic spintronic emitters of ultrabroadband terahertz radiation," Nat. Photonics **10**, 483–488 (2016).
49. C. Vicario, B. Monoszlai, and C. P. Hauri, "GV/m single-cycle terahertz fields from a laser-driven large-size partitioned organic crystal," Phys. Rev. Lett. **112**, 213901 (2014).
50. C. Vicario, A. V. Ovchinnikov, S. I. Ashitkov, M. B. Agranat, V. E. Fortov, and C. P. Hauri, "Generation of 0.9-mJ THz pulses in DSTMS pumped by a Cr:Mg2SiO4 laser," Opt. Lett. **39**, 6632–6635 (2014).
51. https://doi.org/10.6084/m9.figshare.c.4829289